nature communications

Article

https://doi.org/10.1038/s41467-026-69374-4

Ultrafast solvent-modulated roaming mechanism in bromoform revealed by femtosecond X-ray solution scattering

Received: 16 July 2025

Accepted: 28 January 2026

Published online: 09 February 2026

Check for updates

Peiyuan Su[1,10], Jihao Zhang[1,2,10], Hao Wang[3], Yifeng Jiang[3], Sharmistha Paul Dutta[3], Mengxu Li[4], Hazem Yousef[3], Peter Zalden[3], Kai Zhang[5], Ruixue Zhu[2], Xuan Liu[1], Yingqi Wang[6], Sophie E. Canton[7], Diana Bregenholt Jakobsen[3], Doriana Vinci[3], Wenkai Zhang[8] ✉, Jinggang Lan[4] ✉, Tsu-Chien Weng[2] ✉, Wenge Yang[5], Michael Wulff[9], Christopher Milne[3], Dmitry Khakhulin[3] ✉ & Qingyu Kong[1] ✉

Roaming-mediated isomerization is a universal reaction mechanism in photochemistry, yet solvent-dependent pathways of roaming intermediates remain poorly understood, particularly for environmentally relevant halogen compounds involved in ozone depletion. Here, using femtosecond time-resolved X-ray solution scattering, we resolve the solvent-dependent roaming dynamics of $CHBr_3$ in methanol and methylcyclohexane. By combining multi-method experimental analysis, machine learning-assisted ab initio molecular dynamics simulations, and density functional theory calculations, we uncover distinct solvent-steered reaction pathways. In methanol, roaming enhances solute-solvent interactions, leading to solvolysis before a stable isomer forms. In methylcyclohexane, roaming facilitates isomerization to a long-lived iso-$CHBr_2$-Br product. Direct dissociation into $CHBr_2$ + Br competes with both pathways in either solvent. By tracking bond-length oscillations and angular dynamics in real time, we visualize how the condensed-phase environment governs the branching ratio between competing pathways. Our findings establish solute-solvent interactions as key factors controlling roaming-mediated reactions in $CHBr_3$, with broad implications for photochemical outcomes in solution.

Ultraviolet (UV) irradiation of poly-halomethanes releases reactive halogens, driving catalytic ozone depletion in the atmosphere. Among these compounds, bromoform ($CHBr_3$) is the most abundant natural source of bromine (Br_2), a halogen that is over 100 times more destructive to ozone than other halogens[1,2]. As photoactivation is indispensable in Br_2 release from $CHBr_3$[3,4], understanding its photochemical reaction mechanism is essential for elucidating its role in atmospheric photochemistry. In the gas phase, $CHBr_3$ undergoes UV-

[1]Synchrotron Soleil, L'Orme des Merisiers, Saint-Aubin, France. [2]School of Physical Science and Technology, ShanghaiTech University, Shanghai, China. [3]European XFEL, Holzkoppel 4, Schenefeld, Germany. [4]Faculty of Synthetic Biology, Shenzhen University of Advanced Technology, Shenzhen, China. [5]Center for High Pressure Science and Technology Advanced Research, Shanghai, China. [6]Beijing Academy of Quantum Information Sciences, Beijing, China. [7]University of Warsaw, Faculty of Chemistry, Żwirki i Wigury 101, Warsaw, Poland. [8]School of Physics and Astronomy, Applied Optics Beijing Area Major Laboratory, Center for Advanced Quantum Studies, Beijing Normal University, Beijing, China. [9]European Synchrotron Radiation Facility, BP 220, Grenoble, Cedex, France. [10]These authors contributed equally: Peiyuan Su, Jihao Zhang. ✉e-mail: wkzhang@bnu.edu.cn; jinggang.lan@suat-sz.edu.cn; wengzq@shanghaitech.edu.cn; dmitry.khakhulin@xfel.eu; kong@synchrotron-soleil.fr

induced roaming-mediated isomerization in less than 500 fs − a non-traditional dissociation pathway where transiently dissociated fragments reorient via roaming trajectories to form a metastable species, iso-$CHBr_2$–Br, before Br_2 release[5–8]. First identified in formaldehyde, roaming has since been observed in triatomic and tetratomic molecules and has redefined mechanistic understanding across a broad range of photochemical systems[9–15]. A recent study even proposed roaming between water vapor and Criegee intermediates, linking it to atmospheric aerosol formation[16].

However, the current mechanistic picture of $CHBr_3$, derived largely from gas-phase studies, overlooks a critical environmental reality: $CHBr_3$ is primarily emitted from marine biogenic sources, such as phytoplankton and macroalgae[17,18]. Consequently, a fraction of atmospheric $CHBr_3$ resides in condensed-phase environments, including stratospheric aerosols and marine boundary layer droplets[19–21], where solvent interactions are expected to significantly reshape photochemical pathways[22–26]. Indeed, ultrafast optical spectroscopic and theoretical investigations have revealed that the isomerization mechanism is highly dependent on the surrounding environment[5–7,27–30]. The iso-$CHBr_2$-Br can be generated through roaming-mediated isomerization in a few hundreds of femtoseconds or through solvation cage induced germinate recombination of the $CHBr_2$ and Br radicals on picosecond timescales[5,28]. In addition, the lifetime of the iso-CHBr2-Br relies strongly on the properties of solvents; it is metastable in non-polar solvents such as methylcyclohexane and cyclohexane from several nanoseconds to microseconds[28], but relaxes quickly within one nanosecond in polar solvents such as acetonitrile[28] and within a few picoseconds in CCl_4[31].

While optical probes are valuable for tracking excited-state dynamics, their indirect sensitivity to structural changes imposes fundamental limitations. In contrast, time-resolved X-ray solution scattering (TRXSS) offers Ångström-scale spatial resolution, enabling direct visualization of transient structural dynamics during photochemical reactions[32–35]. Previous picosecond TRXSS studies of $CHBr_3$ in methanol could not capture the iso-$CHBr_2$–Br intermediate and instead revealed the formation of CH_3OCHBr_2 and HBr, suggesting an ultrafast solvent-mediated reaction pathway in which the isomer rapidly reacts with the solvent[36]. A similar reaction with water has been observed by time-resolved Raman spectroscopy with a timescale of 1.5 ps[30]. Conversely, the isomer remains stable in methylcyclohexane, as confirmed by our picosecond TRXSS results and previous transient optical spectroscopic studies[28,36]. These previous studies have shown that the stable or hot $CHBr_2$-Br isomer can undergo an O-H insertion/HBr elimination reaction with CH_3OH or H_2O. However, the reported lifetimes of this isomer, less than 1.5 ps in H_2O[30] and less than 100 ps in methanol[36], remain ambiguous. This ambiguity arises partly from the limited temporal resolution of synchrotron-based TRXSS (~100 ps), which cannot access the sub-picosecond timescales where key branching events are likely to occur.

Here, we employ femtosecond TRXSS at the European X-ray Free-electron Laser (EuXFEL), in conjunction with machine-learning-supported ab initio molecular dynamics (AIMD) simulations and density functional theory (DFT) calculations, to directly visualize the photochemical dynamics of $CHBr_3$ in methanol and methylcyclohexane. Our TRXSS results, which are directly sensitive to molecular structures of reacting species in solution, confirm that roaming dynamics initiates universally at the onset of photochemical reaction in both solvents. However, solvent-specific interactions lead to distinct outcomes. In the hydroxyl-rich environment of methanol, solute-solvent interactions quench the roaming-mediated pathway of the hot $CHBr_2$-Br isomer, preventing it from forming the equilibrium stable iso-$CHBr_3$, the hot $CHBr_2$-Br isomer then undergoes subsequent methanolysis reaction, producing secondary CH_3OCHBr_2 and HBr[30,37–39]. In contrast, the nonpolar environment of methylcyclohexane stabilizes the roaming-mediated isomers without solvolysis[26,33]. By determining a ~385 fs lifetime for the hot $CHBr_2$-Br isomer in methanol, our findings reveal how solvent interactions steer $CHBr_3$'s photochemical trajectories from the first few hundreds of femtoseconds, providing atomic-scale insight into how condensed-phase environments determine the fate of photochemical products.

Results and discussions

We excited $CHBr_3$ in methanol and methylcyclohexane using 267 nm UV pulses and conducted TRXSS measurements at the FXE instrument of the EuXFEL (Fig. 1)[40,41]. Photoexcitation of $CHBr_3$ pumps it from the ground state (S_0) to a mixed manifold occupied by both the singlet (S_1) and triplet (T_1, and possibly higher $\tilde{b}^3E$ (T_2) and $\tilde{c}^3A_1$ (T_3)) states, with S_1 likely dominating. Both S_1 and T_1 states are repulsive towards $CHBr_2$· + Br·, with the former having a stronger dissociative character. The T_1 state is populated either directly upon excitation or indirectly via an intersystem crossing (ISC) from the S_1 state and internal conversion from possible higher triplet states[1,5,8,28,42–45]. From T_1, the molecule

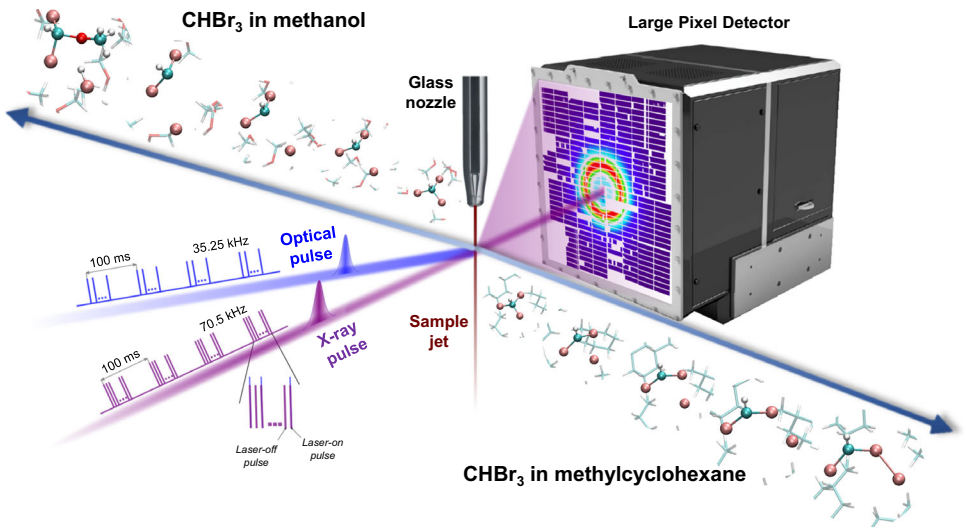

Fig. 1 | Schematic of the TRXSS setup. $CHBr_3$ in methanol or methylcyclohexane is pumped through a cylindrical nozzle, generating a 100 μm-diameter circular liquid jet. The jet is excited by a femtosecond optical pulse at 267 nm, and a delayed X-ray pulse is used to probe the excited liquid. The scattered signals are collected by a Large-Pixel Detector.

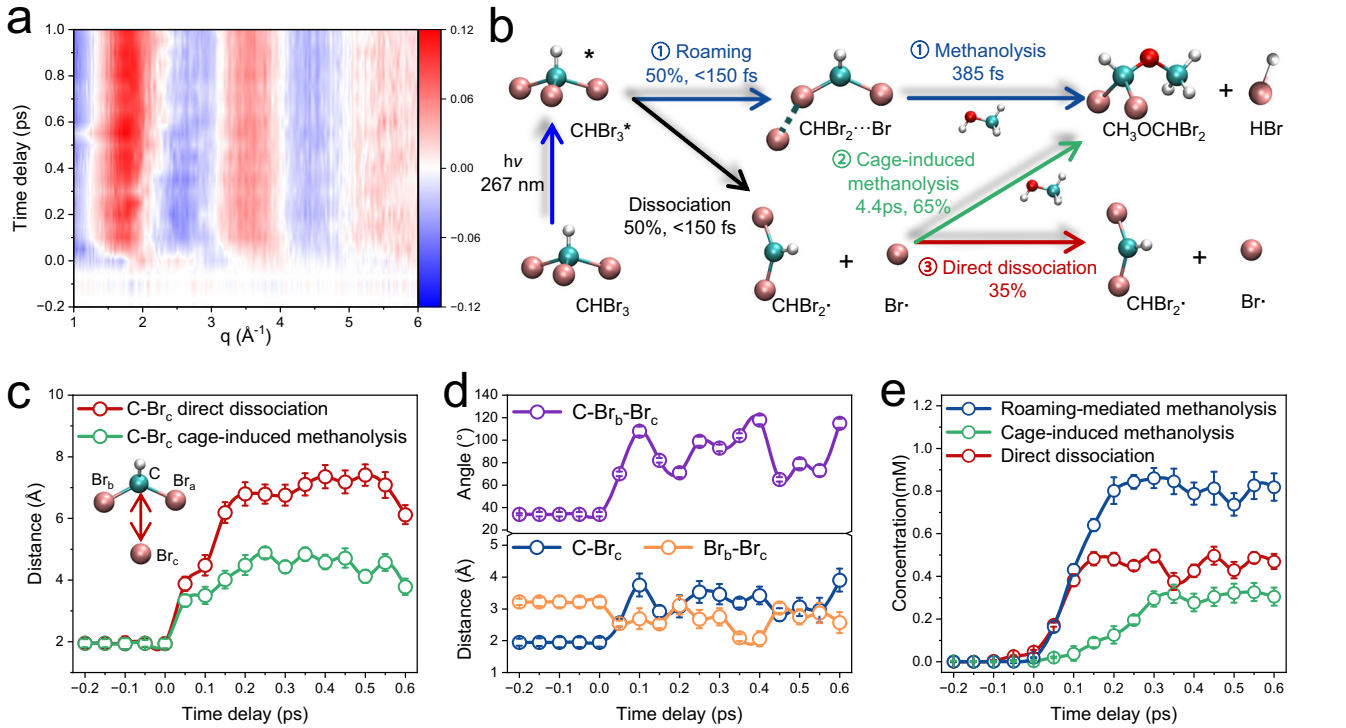

Fig. 2 | Photochemical reaction dynamics of $CHBr_3$ in methanol. a TRXSS measurements on photoexcited $CHBr_3$ in methanol. **b** Proposed photoinduced kinetic model of $CHBr_3$ in methanol. Carbon (cyan), bromine (red-pink), hydrogen (gray), oxygen (red). **c** Atomic motion fitting (AMF) data of the C−Br_c distance in the direct dissociation pathway (red) and cage-induced methanolysis pathway (green). **d** AMF data of the roaming-mediated methanolysis pathway: the C-Br_c distance, Br_b-Br_c distance, and C-Br_b-Br_c angle evolution. **e** Time-dependent transient population changes obtained from AMF analysis. Error bars in panels (**c**–**e**) represent the intervals of the respective optimized fitting parameters, such as interatomic distances, angles, and species concentrations, within which a maximum 5% increase in χ^2 from the global minimum value derived from a set of approximately 1000 randomly generated structures for each time delay.

undergoes structural rearrangement leading to alternative isomeric products[5]. Experimental details are provided in the Supplementary Information (SI).

The TRXSS signals of photoexcited $CHBr_3$ in methanol show clear shifts in momentum transfer (q) within the first ps (Fig. 2a), indicative of ultrafast structural rearrangements. Linear combination fitting (LCF) of theoretical solute/cage signals and experimental solvent scattering to the experimental data[33] rules out isomer formation and identifies CH_3OCHBr_2 and HBr as the primary products after 400 fs (Supplementary Fig. 3; see Supplementary Note 3 for LCF details). The concentration profiles (Supplementary Fig. 3b) reveal ultrafast photodissociation of $CHBr_3$ upon excitation, generating $CHBr_2$ and Br within 150 fs. These species decay rapidly, while the methanolysis products CH_3OCHBr_2 and HBr ($CHBr_3^* + CH_3OH \rightarrow CH_3OCHBr_2 + HBr$) start to appear at delays > 200 fs. This time offset implies the involvement of transient intermediates between excited $CHBr_3^*$ and the methanolysis products, suggesting that the early reaction dynamics extend beyond simple photodissociation and methanolysis pathways. After 300 fs, the decay of $CHBr_2$ and Br slows down markedly, coinciding with a gradual accumulation of CH_3OCHBr_2 and HBr at a comparably reduced rate. This correlation suggests that methanolysis is driven by $CHBr_2$ and Br at late time delays. By 1ps, the concentration of the majority of species begins to stabilize, with the remaining slower methanolysis component persisting for several picoseconds. Notably, the formation of CH_3OCHBr_2 and HBr exhibits biphasic kinetics within the first picosecond, suggesting multiple types of mechanisms in the reaction pathway.

To further elucidate competing photodissociation pathways, we applied Singular Value Decomposition (SVD) to the TRXSS data of photoexcited $CHBr_3$ in methanol (see Supplementary Note 4 for SVD details). The analysis yielded three characteristic timescales: $\tau_1 = 462 \pm 45$ fs, $\tau_2 = 386 \pm 25$ fs, and $\tau_3 = 4.75 \pm 2.4$ ps, with an instrument response function (IRF) of 151 ± 22 fs (Supplementary Figs. 7, 8). The first component ($\tau_1 \approx 460$ fs) corresponds to bulk solvent heating, showing good agreement with both our LCF analysis (471 fs; Supplementary Fig. 5) and previously reported value[46]. The second, somewhat shorter timescale ($\tau_2 = 386$ fs), may be associated with a roaming-mediated process of $CHBr_3$, potentially involving transient structural evolution prior to methanolysis. This timescale is comparable to values reported for similar roaming dynamics[46–48]. The longest timescale ($\tau_3 = 4.75$ ps) appears to correspond to a slower methanolysis pathway involving diffusing $CHBr_2$ and Br fragments. In this case, fragment separation may enable stochastic solute–solvent encounters that ultimately lead to the formation of CH_3OCHBr_2 and HBr.

Preliminary analysis using LCF and SVD suggested the presence of multiple reaction pathways and provided initial estimates for their lifetimes and branching ratios. Based on these parameters and according to the proposed scheme in Fig. 2b, a kinetic model was constructed, which served as the basis for global fitting analysis (GFA, see Supplementary Note 5 for details). By fitting TRXSS data to this model, GFA refined the initial estimates and offered further support for the proposed framework. Photoexcitation triggers ultrafast C−Br bond cleavage (<150 fs), producing $CHBr_2$ and Br, which subsequently bifurcate into two competing pathways: (1) Roaming-mediated methanolysis ($52 \pm 18\%$ branching), where CH_3OCHBr_2 and HBr are formed within 385 ± 80 fs; (2) Direct dissociation ($48 \pm 16\%$ branching), where 65% of $CHBr_2$ and Br undergo solvent-cage-induced methanolysis in 4.4 ± 0.9 ps, while the remaining 35% persist beyond the nanosecond timescale[27,28,36]. The dissociation-to-methanolysis ratio (1:2.5) at 1 ps is comparable to previous synchrotron-based TRXSS results[36]. The kinetic traces derived from GFA show good agreement with those obtained from LCF (Supplementary Fig. 11a) as well.

Previous study indicated that $CHBr_3$ isomerization passes through the S_1/S_0 conical intersection in ~29 fs[5], while our data illustrate that the resulting hot $CHBr_2$-Br isomer reacts with methanol at ~385 fs. This prolonged timescale confirms that the methanolysis reaction occurs after the system undergoes an electronic transition from the excited state to the S_0 ground state.

With the kinetic model, we aimed to characterize the transient intermediates bridging the excited $CHBr_3^*$ and the methanolysis products. These hot intermediates are likely not at the local minimum on the potential energy surface (PES), which are challenging to model theoretically. To address this point, we performed atomic motion fitting (AMF) of the TRXSS data over the critical first 600 fs with numerically constructed transient structures involving various geometries along the reaction PES[8]. This AMF approach (see Supplementary Note 6 for details) enabled direct insight into ultrafast structural reorganizations along distinct photoreaction coordinates. Specifically, we considered structural configurations representative of the three proposed mechanistic channels – roaming-mediated methanolysis, direct dissociation, and cage-induced methanolysis – as guided by the GFA results. AMF was focused on transient changes in key reactive structural motifs involving carbon and bromine atoms, including C–Br bond lengths, Br–C–Br bond angles, and Br–C–Br–Br dihedral angles[8]. To comprehensively explore the relevant configurational space, chemically reasonable ranges were defined for each degree of freedom. A random sampling approach was employed to generate ~1,000 structurally diverse geometries within these constraints[46].

The dissociation pathway exhibits two distinct behaviors (Fig. 2c). In a direct dissociation reaction, C–Br_c increases from 1.94 Å to ~6.5 Å by 150 fs. In cage-induced methanolysis, limited C–Br_c separation (~4.5 Å at 200 fs) and unexpected contraction to ~3.5 Å by 600 fs illustrate the collisions between the fragments and solvent molecules, facilitating solvent-mediated reorganization to CH_3OCHBr_2 and HBr.

In roaming-mediated methanolysis (Fig. 2d), the ground state $CHBr_3$ (C–Br_c: 1.94 Å; Br_c–Br_b: 3.22 Å; C–Br_b–Br_c: 34°) undergoes ultrafast structural reorganization within 100 fs after excitation: C–Br_c bond elongates to 3.75 Å, while Br_c–Br_b contracts to ~2.6 Å, accompanied by a sharp expansion of the C–Br_b–Br_c angle to 108°. These changes in internal coordinates indicate that the $CHBr_2$ and Br fragments undergo a roaming motion, which forms a hot $CHBr_2$-Br isomer. Subsequent oscillations (100–600 fs) in bond lengths (C–Br_c: 3-3.8 Å; Br_c–Br_b: 2.2-3 Å) and C–Br_b–Br_c angle (80–120°) of the hot $CHBr_2$-Br isomer enhance methanol encounters, progressively driving methanolysis. Similar roaming-mediated behaviors have been observed in previous studies[5,8]. Detailed structural dynamics of $CHBr_3$ in methanol at early time delays are displayed in Supplementary Fig. 13.

The transient population dynamics of the key structures involved in the three mechanistic pathways are shown in Fig. 2e. The concentrations of the representative structures associated with the direct dissociation and roaming-mediated methanolysis pathways rapidly stabilized at 0.5 mM and 0.8 mM, respectively, within 200 fs. In contrast, the population associated with the cage-induced methanolysis pathway gradually increased to ~0.3 mM at 300 fs, suggesting a slower interaction with the cage environment. The combined AMF-GFA analysis resolves the transient structural dynamics during the reaction's critical initiation phase (Supplementary Fig. 14). This approach provides substantially better agreement between theoretical and experimental scattering signals (Supplementary Fig. 14c), with residuals (Supplementary Fig. 14b) markedly reduced at early times compared to pure global fitting (Supplementary Fig. 11c).

Figure 3a shows the experimental TRXSS signal of photoexcited $CHBr_3$ in methylcyclohexane. The LCF analysis (Supplementary Fig. 4) reveals the formation of the $CHBr_2$-Br isomer and direct dissociation products $CHBr_2$ + Br, with both populations peaking within 400 fs. Notably, the $CHBr_2$-Br isomer appears ~100 fs later than the dissociation products, indicating precursor-mediated isomer formation[49]. This time delay results from the formation of the T_1 potential energy surface, which is populated either directly upon excitation or indirectly via ISC from S_1 state and internal conversion from higher triplet excited states within the mixed excitation manifold. The concurrent temporal evolution of the product concentrations demonstrates that the growths of the dissociated radicals and the $CHBr_2$-Br isomer are coupled over picoseconds.

We performed SVD analysis of the TRXSS data in Fig. 3a, isolating a dominant component (Supplementary Fig. 9). Fitting the corresponding first right singular vector (RSV_1) (Supplementary Fig. 10) gave an IRF of 153 ± 33 fs, matching our methanol measurements. Two lifetimes were resolved: a fast component (<150 fs) and a slower one (373 ± 66 fs), corresponding to different product formation timescales.

The fittings (solid lines, Supplementary Fig. 4) of the LCF-derived kinetics for the two reaction pathways confirm photoproduct formation within the instrument resolution (150 fs). This observation rules out a stable precursor and supports a roaming-mediated isomerization mechanism involving transient structural rearrangements[26,46], although slightly delayed compared to the competing direct dissociation. The fitted lifetime agrees with the shorter component resolved by SVD. LCF further quantified solvent heating dynamics, revealing a single-exponential temperature rise (408 ± 27 fs, Supplementary Fig. 6), which matches the slower SVD component (373 ± 66 fs). Together, LCF and SVD analysis show that both dissociation and isomerization proceed on the ultrafast timescale, though isomer formation involves a more complex pathway, with a delayed appearance due to roaming-mediated rearrangements (Supplementary Fig. 4). The observed ~100 fs delay reflects the early-time electronic and nuclear dynamics of the spin-mixed n(Br)→σ^*(C–Br) excited-state manifold populated at 267 nm. Following photoexcitation, the wavepacket rapidly departs the Franck-Condon region, undergoes ultrafast spin equilibration and internal conversion among nearly degenerate singlet and triplet states, and approaches regions of strong nonadiabatic coupling between T_1 and S_0. Formation of the $CHBr_2$-Br roaming configuration thus occurs only after this joint electronic–nuclear evolution, naturally accounting for the measured temporal offset.

To probe the transient structural evolution leading to isomer and radical formation, we analyzed the TRXSS data within the first 600 fs using AMF method (Supplementary Fig. 18). In the direct dissociation pathway (Fig. 3c), C–Br_c bond elongation occurs in three distinct phases: 0-50 fs, rapid elongation from 1.94 Å to 4.39 Å (0.049 Å/fs), approaching the C–Br dissociation threshold. 50–150 fs, slowed extension to 5.8 Å (0.0141 Å/fs), indicating solvent drag effects. 150-300 fs, further deceleration to 6.5 Å (0.0047 Å/fs) as energy dissipates through solvent collisions. Beyond 300 fs, the separation distance of C–Br_c reaches a plateau, indicating loss of geminate correlation between $CHBr_2$ and Br, which is in close agreement with LCF-derived product formation timescales.

In contrast, isomerization proceeds via changes in three primary coordinates: C–Br_c and Br_c–Br_b distances, and the C–Br_b–Br_c angle (Fig. 3d). 0–50 fs, the angle increases from 34° to 57° (0.46°/fs), while C–Br_c elongates to 3.31 Å (0.0274 Å/fs) and Br_c–Br_b expands to 3.93 Å (0.0142 Å/fs), consistent with an early-time reorientation of the $CHBr_2$ and Br fragments. 50-100 fs, the angle rapidly rises to 118° (1.22°/fs), while Br_c–Br_b sharply contracts to 2.4 Å (-0.031 Å/fs), forming a hot $CHBr_2$-Br isomer. 100-150 fs, the angle decreases to 98° (−0.46°/fs), and Br_c–Br_b modestly increases to 2.67 Å (0.0054 Å/fs), indicating early stabilization of the hot $CHBr_2$-Br isomer. The observed non-monotonic dynamics trace a roaming-mediated transition to a vibrationally hot configuration by 150 fs (C–Br_c ≈ 3.44 Å, Br_c–Br_b ≈ 2.67 Å, ∠C–Br_b–Br_c ≈ 95°), thereby confirming that a delayed structural rearrangement precedes and ultimately leads to the formation of a hot isomer. Our observations are consistent with previous reports on

https://doi.org/10.1038/s41467-026-69374-4

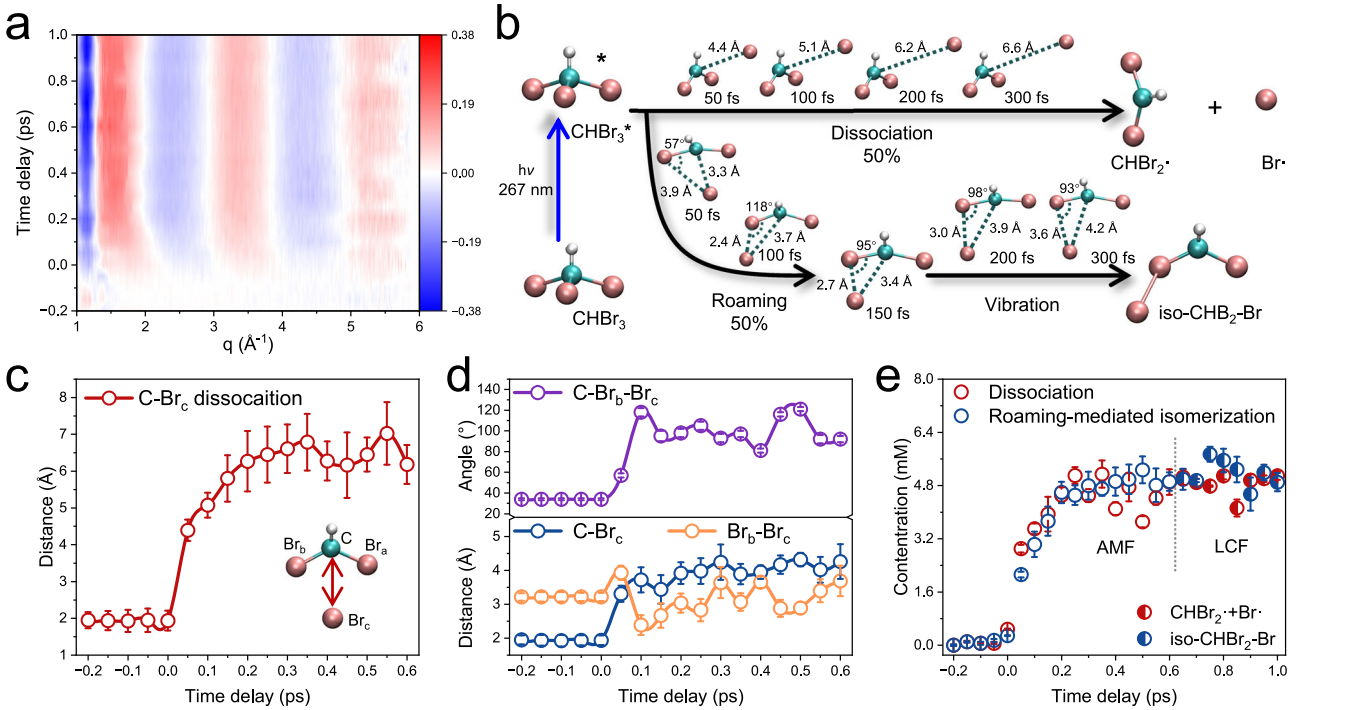

Fig. 3 | Photochemical reaction dynamics of $CHBr_3$ in methylcyclohexane. **a** TRXSS data of photoexcited $CHBr_3$ in methylcyclohexane. **b** Proposed kinetic model for photoexcited $CHBr_3$ in methylcyclohexane. **c** AMF obtained C–Br bond distance evolution in the direct dissociation pathway. **d** AMF obtained structural dynamics for the roaming-mediated isomerization pathway: C–Br_c distance, Br_b-Br_c distance, and C-Br_b-Br_c angle. Error bars represent the intervals of the optimized structural parameters, such as interatomic distances and angles, that result in a maximum 5% increase in χ^2 from the global minimum value, derived from approximately 1000 randomly generated structures for each time delay. **e** Time-dependent population changes of transient species within 600 fs obtained from AMF analysis and concentrations of dissociation products and isomers after 600 fs obtained from LCF analysis. Error bars represent the intervals of the species concentrations obtained using selected optimized structures in AMF analysis for time delays earlier than 600 fs. For time delays beyond 600 fs, error bars indicate one standard deviation of the concentrations for each component, extracted from LCF over five independent measurements.

roaming-mediated dynamics in similar systems[5,8]. The subsequent weak oscillations (150–600 fs) reflect vibrational relaxation around the stabilized isomer.

The roaming dynamics on T_1 ultimately relax to the ground-state (S_0) surface via T_1/S_0 interaction, as evidenced by our DFT calculations (Supplementary Fig. 27; see Supplementary Note 8 for details). Our structural analysis shows that the Br atom and $CHBr_2$ fragment roaming most likely proceeds on T_1 surface within the first 100 fs and yields a hot $CHBr_2$-Br isomer by ~150 fs in the S_0 state. Consequently, the weak oscillations observed from 150 to 600 fs, which reflect vibrational relaxation around the stabilized isomer, are assigned to dynamics on the S_0 potential energy surface.

AMF also quantifies the temporal evolution of key structural populations (Fig. 3e). Both pathways contribute simultaneously at early time delays, reconciling the initial temporal (~100 fs) offset between isomerization and dissociation. The excellent agreement between LCF, AMF, and experimental TRXSS data (Supplementary Fig. 18) robustly supports these mechanistic conclusions.

To elucidate the solvent-dependent roaming behavior of $CHBr_3$ observed experimentally, we complemented our studies with ab initio molecular dynamics (AIMD) simulations and density functional theory (DFT) calculations in methanol and methylcyclohexane. These calculations offer atomistic insights into the mechanistic origins of the solvent-controlled reactivity contrast.

We employed the ab initio molecular dynamics (AIMD) based on the unrestricted Kohn-Sham method, combined with machine learning potentials, to probe the triplet excited-state (T_1) dynamics of $CHBr_3$ in methanol and methylcyclohexane[5,28,45] (see Supplementary Note 7 for details). Our simulations were conducted on the T_1 excited state due to the ultrafast ISC from S_1 to T_1, which makes the triplet excited state the dominant channel for the subsequent photochemical dynamics, specifically relevant for the roaming process. Correlation plots of interatomic distances, specifically Br_a–Br_c versus Br_b–Br_c (Fig. 4a, b), effectively capture the trajectory-dependent behavior of the dissociating bromine atom (Br_c). Trajectories along the diagonal correspond to symmetric dissociation, where Br_a and Br_b remain equidistant from Br_c, indicative of direct dissociation and negligible roaming. Off-diagonal excursions indicate a transient asymmetry in the Br-Br separations, signifying a reorientation of both the $CHBr_2$ and Br fragments. These excursions are clear signatures of $CHBr_2$-Br isomer structures formed via roaming-mediated dynamics, and their subsequent oscillations represent the vibrational motion of these transient intermediates[5,8].

In methanol (Fig. 4a), simulations reveal a rapid dissociation of the Br_c radical from the $CHBr_2$ fragment. A representative trajectory (red trace) illustrates structural evolution at 50 fs (point B), 200 fs (point C), and 300 fs (point D). Within the first 50 fs, rapid Br_c dissociation occurs, followed by distinctive roaming behavior that leads to transient configurations. Notably, this involves an expansion of the C–Br_b–Br_c angle from 32° to 104° and an increase in the Br_a–Br_c distance from 3.2 Å to 5.4 Å, indicative of roaming-mediated reaction. Although explicit solvent coordination between $CHBr_3$ and methanol was not directly modeled due to computational constraints, the simulated structural dynamics align well with the experimental observations (Supplementary Fig. 21). The simulation also illustrates a significantly smaller solvation cage for $CHBr_3$ in methanol (Supplementary Fig. 23), indicating a stronger solute-solvent interaction. These AIMD results suggest that vibrational motions of isomer-like structures facilitate methanolysis by promoting solute–solvent collisions.

https://doi.org/10.1038/s41467-026-69374-4

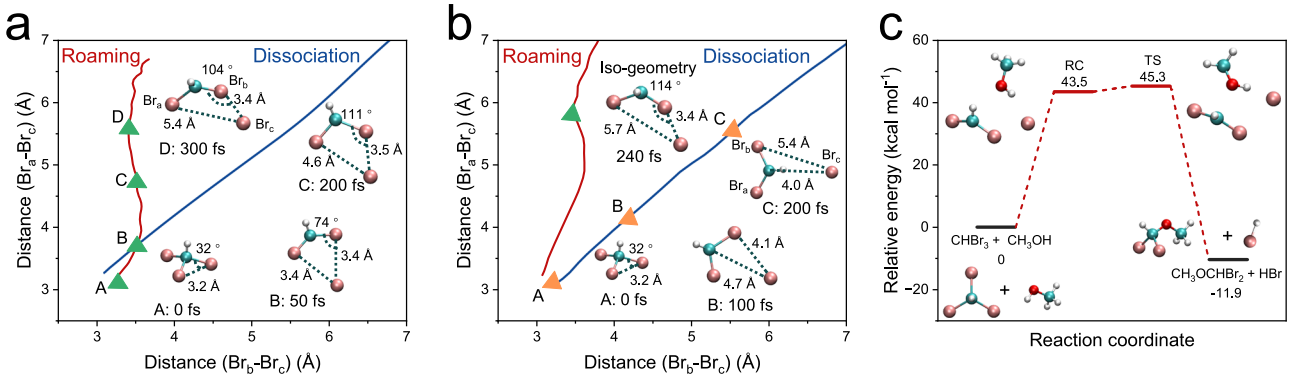

Fig. 4 | Ab initio molecular dynamics (AIMD) Simulations and DFT calculation. **a**, **b** Correlation between the dissociating Br_c and the retained Br_a and Br_b in the $CHBr_2$ fragment. **a** Trajectories of $CHBr_3$ in methanol. Green triangles indicate representative structures at 0 fs, 50 fs, 200 fs, and 300 fs along the roaming pathway. **b** Trajectories of $CHBr_3$ in methylcyclohexane. The green triangle represents the geometry close to the stable isomer along the roaming pathway at 240 fs. Orange triangles correspond to structures at 0 fs, 100 fs, and 200 fs during the dissociation process. The time-dependent distances between Br_c and Br_a/Br_b reflect structural reorganization during the reaction. **c** DFT calculated potential energy surfaces for the roaming-mediated methanolysis pathway.

Simulations of $CHBr_3$ in methylcyclohexane (highlighted in red in Fig. 4b) reveal pronounced roaming-mediated isomerization. By 240 fs, the geometry converges distinctly toward iso-$CHBr_2$-Br, consistent with the experimentally determined isomerization timescale. Simultaneously, in the direct dissociation channel, the Br_b–Br_c distance increases from 3.2 Å to 5.4 Å by 200 fs, while the C–Br_c distance shortens from 4.7 Å (100 fs) to 4.0 Å (200 fs), indicating rotation of the $CHBr_2$ fragment around the Br_a–Br_b axis. A detailed comparison between AIMD simulations and AMF results further confirms our experimental findings (Supplementary Fig. 22).

To evaluate the influence of solvent-cage environments, we analyzed the simulated radial distribution function (RDF) of ground-state $CHBr_3$ in methanol and methylcyclohexane (Supplementary Fig. 23). The cage radius in methanol (3.1 Å) is significantly smaller than in methylcyclohexane (5.66 Å), indicating a more confined environment in methanol. This distinction explains the observed mechanistic differences: the spacious, gas-phase-like cage in methylcyclohexane facilitates roaming-mediated isomerization, while the compact hydroxyl-rich environment of methanol hinders relaxation of the hot $CHBr_2$-Br isomer to the equilibrated ground-state iso-$CHBr_3$ and instead promotes methanolysis.

DFT calculations reveal the energetic landscape of the roaming-mediated methanolysis reaction (Fig. 4c). The dissociated Br atom dynamically reorients relative to the $CHBr_2$ radical and the methanol molecule, eventually forming a stable reaction complex (RC). This RC overcomes a modest 1.8 kcal/mol energy barrier via a transition state, yielding CH_3OCHBr_2 and HBr (Supplementary Figs. 24–26 and Supplementary Table 2 for detailed structural parameters and reaction dynamics). Together with experimental results, these computations establish a unified mechanistic picture that explains the solvent-dependent competition between dissociation, isomerization, and methanolysis pathways.

This study provides direct structural evidence of how solvent interactions govern the ultrafast photochemistry of halomethanes. By combining femtosecond TRXSS and advanced theoretical simulations, we demonstrate that $CHBr_3$ undergoes roaming-mediated isomer formation within 150 fs in both methanol and methylcyclohexane—establishing this non-classical pathway as a universal feature in the condensed phase. The subsequent fate of the roaming intermediates is then determined by the solvent environment. The solvent interactions and cage effect in methanol facilitate the ultrafast methanolysis, leading to the formation of CH_3OCHBr_2 and HBr within ~385 fs, while the inert methylcyclohexane solvent stabilizes the roaming isomer. The synergy between femtosecond TRXSS and theoretical simulations emerges as a powerful approach for resolving solvent-dependent structural dynamics. Combined with our earlier work[36], these findings established a complete mechanistic picture of $CHBr_3$ photochemical dynamics in solution from femtosecond bond cleavage to microsecond bromine (Br_2) formation. These findings highlight the pivotal role of solvent interactions in steering ultrafast photochemical pathways, offering a mechanistic framework for understanding the photochemical reactivity of environmentally relevant species in complex media, such as aerosols, droplets, and biological interfaces.

Methods

Femtosecond time-resolved X-ray solution scattering (fs-TRXSS)

Time-resolved X-ray solution scattering (TRXSS) experiments were performed at the FXE instrument of the European XFEL using a pump-probe configuration[40,41]. Solutions of bromoform in methanol or methylcyclohexane (40 mM) were used to probe reaction dynamics, while 4-bromo-4′-(N, N-diethylamino)-azobenzene (2 mM) in the same solvents was used to measure solvent heating signals[50]. Photoexcitation was achieved with 267 nm laser pulses of 70 fs duration, focused to 70 × 70 μm² (FWHM) at the liquid jet. X-ray probe pulses (~50 fs) were focused to 15 × 15 μm² (FWHM), and scattered signals were recorded using a Large Pixel Detector (LPD) positioned 238 mm from the jet. Momentum transfer was defined as $q = 4\pi\sin(\theta)/\lambda$ (where θ is the scattering angle and λ the X-ray wavelength) and reached 6 Å^{-1}. Two-dimensional scattering patterns of $CHBr_3$ in methanol or methylcyclohexane were collected over time delays ranging from −0.2 ps to 1 ps with a step size of 50 fs. To probe the long-time kinetics, scattering data were acquired at selected longer delays up to 10 ps (Supplementary Figs. 3 and 4). Two-dimensional scattering patterns of the dye were recorded at a fixed delay of 10 ps. Each dataset was measured in five independent runs to ensure reproducibility. Detailed information on data acquisition is provided in Supplementary Note 1.

Extraction of difference scattering signals

One-dimensional scattering profiles $S(q)$ were obtained by azimuthal integration of 2D scattering maps. Difference scattering signals $\Delta S(q)$ were computed for each laser-on/off pulse pair and averaged across all pairs to give the final difference profile. The averaged $\Delta S(q)$ was weighted by q (as $q\Delta S(q)$) to highlight high-angle features.

2D maps were decomposed into isotropic and anisotropic components using a second-order Legendre polynomial expansion[51]. The isotropic component reflects solute structural changes and solute–solvent interactions (Figs. 2a, 3a). The anisotropic component reflects ultrafast solvent reorientation along the laser polarization axis (Supplementary Fig. 1a, c). The temporal evolution of the anisotropic signals was fitted with a Gaussian–exponential model to determine

solvent reorientation times and the instrument response function (IRF) (Supplementary Fig. 1b, d). Details of signal extraction and processing are provided in Supplementary Note 1.

Linear combination fitting analysis of difference scattering signals

The isotropic difference scattering signals were first analyzed using Linear Combination Fitting (LCF) to extract the time-dependent coefficients of different transient species. The data were modeled as a linear combination of solute, cage (the solute-solvent interaction), and solvent-heating contributions. The solvent-heating term $\left(\frac{\partial S}{\partial T}\right)_\rho$ was derived from the TRXSS measurement of azo-dye[50]. Theoretical scattering curves for all species were calculated based on density functional theory optimized structures and molecular dynamics simulated cages[36,52–55]. LCF was performed at each time delay by minimizing the figure of merit (χ^2) following the formula:

$$\chi^2 = \sum_{i=1}^{n} \left(\frac{\Delta S_{\text{theory}}(q_i) - \Delta S_{\text{experiment}}(q_i)}{\sigma_i} \right)^2$$

where σ_i is the standard deviation of the scattering signal at the i-th q value for the given time delay. The full description of the LCF strategy is provided in Supplementary Note 3.

Singular value decomposition analysis of difference scattering signals

Singular value decomposition (SVD) was applied to the isotropic TRXSS data to determine the number of statistically significant components and their associated kinetics. The significance of components was evaluated through singular value magnitudes and the autocorrelation of the singular vectors. The right singular vectors (RSVs) were modeled using multi-exponential functions convolved with IRF. Further details on the SVD and RSV fitting are provided in Supplementary Note 4.

Global fitting analysis of difference scattering signals

Global fitting analysis (GFA) was performed to construct a kinetic model that consistently describes the TRXSS signals of $CHBr_3$ in methanol across all momentum-transfer space and time-delay ranges. The kinetic model was constructed by integrating LCF concentration profiles with time constants identified by SVD. This approach provides physically informed constraints on both the reaction pathways and the associated time scales. The model treats roaming-mediated isomerization and direct bond dissociation as competing parallel channels, therefore containing multiple adjustable parameters, including the branching ratio between the two dissociation pathways, the characteristic time constants associated with secondary reaction steps, and the fraction of unreacted species. A total of 500 sets of initial parameters for the model were randomly sampled within these bounds and used as initial points for global fitting. Detailed kinetic fitting process and the parameter sampling strategy are described in Supplementary Note 5.

Atomic motion fitting of early (≤600 fs) difference scattering signals

To resolve ultrafast structural evolution, Atomic Motion Fitting (AMF) was employed to refine transient molecular geometries within the first 600 fs. Transient structures were constructed by varying heavy-atom positions (C and three Br atoms) while constraining the hydrogen atom, which has a negligible X-ray scattering contribution. This strategy reduces the number of independent degrees of freedom while preserving the physically relevant structural changes. The geometry was parameterized using spherical coordinates to maintain molecular symmetry. Structural models representing the distinct pathways identified by GFA were refined by minimizing the figure of merit χ^2. Structural uncertainties were estimated by randomly sampling 1000 initial structures at each time delay and retaining optimized geometries with χ^2 values within a narrow threshold within 1.05 times the global minimum[46]. A comprehensive description of the structural representation and fitting constraints is provided in Supplementary Note 6. All LCF, SVD, GFA, and AMF were performed using MATLAB R2024a.

Ab-initio molecular dynamics simulations

Ab initio molecular dynamics (AIMD) simulations were performed to investigate the photochemical dynamics of $CHBr_3$ in solution. Electronic-structure calculations were carried out using the van der Waals–corrected hybrid functional PBEh(40%)-rVV10[56]. Simulations were carried out for $CHBr_3$ in methanol and methylcyclohexane at room temperature, considering both the electronic ground state and the triplet excited state.

Machine-learning potentials based on the MACE framework[57] were trained on configurations sampled from ground-state and triplet-state (T_1) AIMD simulations and used to enable long-timescale molecular dynamics. Ground-state trajectories of $CHBr_3$ solvated in methanol and methylcyclohexane were propagated for 100 ps under NPT conditions at 300 K and 1 bar. Excited-state dynamics were initiated from configurations sampled along the equilibrated ground-state trajectories and propagated on the triplet-state potential energy surface for 2 ps in the NVE ensemble. Molecular dynamics simulations were performed with i-PI, and electronic-structure calculations were carried out using CP2K. Details of the simulation parameters are provided in Supplementary Note 7.

Density functional theory (DFT) calculations

DFT calculations were performed to investigate the roaming-mediated reaction between bromoform and methanol. Geometry optimizations, vibrational frequency analyses, and transition-state searches were carried out using Gaussian 16 at the CAM-B3LYP/6-311++G(3df,3pd) level of theory[58–60] (Supplementary Fig. 24). Transition states were validated by frequency and intrinsic reaction coordinate (IRC) calculations connecting the corresponding reactants and products (Supplementary Figs. 25, 26). Potential energy profiles along the IRC were calculated for the S_0 and T_1 surfaces of $CHBr_3$ at the same level of theory (Supplementary Fig. 27). Detailed computational procedures and structural parameters are provided in Supplementary Note 8.

Data availability

Source data used to generate all figures in the main text and Supplementary Information are provided. This includes the processed data required to reproduce the key findings of this study. The raw TRXSS images are archived on the EuXFEL data storage server and are available from the corresponding author upon request. Source data are provided with this paper.

References

1. Peterson, K. A. & Francisco, J. S. Should bromoform absorb at wavelengths longer than 300 nm? *J. Chem. Phys.* **117**, 6103–6107 (2002).
2. Foster, K. L. et al. The role of Br2 and BrCl in surface ozone destruction at polar sunrise. *Science* **291**, 471–474 (2001).
3. Huang, H.-Y. et al. Molecular elimination of Br2 in 248 nm photolysis of bromoform probed by using cavity ring-down absorption spectroscopy. *J. Chem. Phys.* **121**, 5253–5260 (2004).
4. Xu, D., Francisco, J. S., Huang, J. & Jackson, W. M. Ultraviolet photodissociation of bromoform at 234 and 267 nm by means of ion velocity imaging. *J. Chem. Phys.* **117**, 2578–2585 (2002).
5. Mereshchenko, A. S., Butaeva, E. V., Borin, V. A., Eyzips, A. & Tarnovsky, A. N. Roaming-mediated ultrafast isomerization of geminal

tri-bromides in the gas and liquid phases. *Nat. Chem.* **7**, 562–568 (2015).
6. Borin, V. A., Matveev, S. M., Budkina, D. S., El-Khoury, P. Z. & Tarnovsky, A. N. Direct photoisomerization of CH(2)I(2)vs. CHBr(3) in the gas phase: a joint 50 fs experimental and multireference resonance-theoretical study. *Phys. Chem. Chem. Phys.* **18**, 28883–28892 (2016).
7. Godara, S. & Paranjothy, M. Competing molecular and radical pathways in the dissociation of halons via direct chemical dynamics simulations. *J. Phys. Chem. A* **123**, 8527–8535 (2019).
8. Hoffmann, L. et al. UV-induced reaction pathways in bromoform probed with ultrafast electron diffraction. *J. Am. Chem. Soc.* https://doi.org/10.1021/jacs.4c07165 (2024).
9. Townsend, D. et al. The roaming atom: straying from the reaction path in formaldehyde decomposition. *Science* **306**, 1158–1161 (2004).
10. Bowman, J. M. & Houston, P. L. Theories and simulations of roaming. *Chem. Soc. Rev.* **46**, 7615–7624 (2017).
11. Endo, T. et al. Capturing roaming molecular fragments in real time. *Science* **370**, 1072–1077 (2020).
12. Quinn, M. S. et al. Rotational resonances in the H2CO roaming reaction are revealed by detailed correlations. *Science* **369**, 1592–1596 (2020).
13. Westermayr, J. et al. Deep learning study of tyrosine reveals that roaming can lead to photodamage. *Nat. Chem.* **14**, 914–919 (2022).
14. Liu, T. et al. OH roaming and beyond in the unimolecular decay of the methyl-ethyl-substituted criegee intermediate: observations and predictions. *J. Am. Chem. Soc.* **145**, 19405–19420 (2023).
15. Li, Z. et al. Roaming in highly excited states: The central atom elimination of triatomic molecule decomposition. *Science* **383**, 746–750 (2024).
16. Liu, Y. et al. Reactivity of syn-CH3CHOO with H2O enhanced through a roaming mechanism in the entrance channel. *Nat. Chem.*, https://doi.org/10.1038/s41557-025-01798-9 (2025).
17. Gschwend, P. M., MacFarlane, J. K. & Newman, K. A. Volatile halogenated organic compounds released to seawater from temperate marine macroalgae. *Science* **227**, 1033–1035 (1985).
18. Sturges, W. T., Cota, G. F. & Buckley, P. T. Bromoform emission from Arctic ice algae. *Nature* **358**, 660–662 (1992).
19. Carpenter, L. J., Archer, S. D. & Beale, R. Ocean-atmosphere trace gas exchange. *Chem. Soc. Rev.* **41**, 6473–6506 (2012).
20. Aschmann, J. & Sinnhuber, B. M. Contribution of very short-lived substances to stratospheric bromine loading: uncertainties and constraints. *Atmos. Chem. Phys.* **13**, 1203–1219 (2013).
21. Hamer, P. D. et al. Cloud-scale modelling of the impact of deep convection on the fate of oceanic bromoform in the troposphere: a case study over the west coast of Borneo. *Atmos. Chem. Phys.* **21**, 16955–16984 (2021).
22. Vester, P. et al. Tracking structural solvent reorganization and recombination dynamics following e(-) photoabstraction from aqueous I(-) with femtosecond x-ray spectroscopy and scattering. *J. Chem. Phys.* **157**, 224201 (2022).
23. Vong, A., Mei, K. J., Widmer, D. R. & Schwartz, B. J. Solvent control of chemical identity can change photodissociation into photoisomerization. *J. Phys. Chem. Lett.* **13**, 7931–7938 (2022).
24. Nimmrich, A. et al. Solvent-dependent structural dynamics in the ultrafast photodissociation reaction of triiodide observed with time-resolved x-ray solution scattering. *J. Am. Chem. Soc.* **145**, 15754–15765 (2023).
25. Qiu, Z. & Neumann, C. N. Influence of cage effects in directing the outcome of c-x bond forming reactions. *ACS Org. Inorg. Au* **4**, 1–25 (2024).
26. Wang, C. et al. Different timescales during ultrafast stilbene isomerization in the gas and liquid phases revealed using time-resolved photoelectron spectroscopy. *Nat. Chem.* **14**, 1126–1132 (2022).
27. Carrier, S. L., Preston, T. J., Dutta, M., Crowther, A. C. & Crim, F. F. Ultrafast observation of isomerization and complexation in the photolysis of bromoform in solution. *J. Phys. Chem. A* **114**, 1548–1555 (2010).
28. Pal, S. K., Mereshchenko, A. S., Butaeva, E. V., El-Khoury, P. Z. & Tarnovsky, A. N. Global sampling of the photochemical reaction paths of bromoform by ultrafast deep-UV through near-IR transient absorption and ab initio multiconfigurational calculations. *J. Chem. Phys.* **138**, 124501 (2013).
29. Bhattacharyya, S. et al. Two- and three-body fragmentation of multiply charged tribromomethane by ultrafast laser pulses. *Phys. Chem. Chem. Phys.* **24**, 27631–27644 (2022).
30. Kwok, W. M. et al. Water-catalyzed dehalogenation reactions of isobromoform and its reaction products. *J. Am. Chem. Soc.* **126**, 3119–3131 (2004).
31. Preston, T. J., Shaloski, M. A. & Crim, F. F. Probing the photoisomerization of CHBr3 and CHI3 in solution with transient vibrational and electronic spectroscopy. *J. Phys. Chem. A* **117**, 2899–2907 (2013).
32. Chergui, M. & Collet, E. Photoinduced structural dynamics of molecular systems mapped by time-resolved x-ray methods. *Chem. Rev.* **117**, 11025–11065 (2017).
33. Ma, L. et al. Revealing the reaction path of UVC bond rupture in cyclic disulfides with ultrafast x-ray scattering. *Sci. Adv.* **11**, eadp9175 (2025).
34. Biasin, E. et al. Direct observation of coherent femtosecond solvent reorganization coupled to intramolecular electron transfer. *Nat. Chem.* **13**, 343–349 (2021).
35. Powers-Riggs, N. E. et al. Characterization of deformational isomerization potential and interconversion dynamics with ultrafast x-ray solution scattering. *J. Am. Chem. Soc.* **146**, 13962–13973 (2024).
36. Kong, Q. et al. Solvent-dependent complex reaction pathways of bromoform revealed by time-resolved X-ray solution scattering and X-ray transient absorption spectroscopy. *Struct. Dyn.* **6**, 064902 (2019).
37. El-Khoury, P. Z. et al. Photochemistry of iodoform in methanol: formation and fate of the iso-CHI2-I photoproduct. *Chemphyschem* **10**, 1895–1900 (2009).
38. Marcellini, M. et al. Transient isomers in the photodissociation of bromoiodomethane. *J. Chem. Phys.* **148**, 134307 (2018).
39. Guan, X. et al. Ultraviolet photolysis of ch2i2 in methanol: o–h insertion and hi elimination reactions to form a dimethoxymethane product. *J. Phys. Chem. A* **109**, 1247–1256 (2005).
40. Khakhulin, D. et al. Ultrafast X-ray Photochemistry at European XFEL: Capabilities of the Femtosecond X-ray Experiments (FXE) Instrument. *Applied Sciences* **10**, https://doi.org/10.3390/app10030995 (2020).
41. Galler, A. et al. Scientific instrument Femtosecond X-ray Experiments (FXE): instrumentation and baseline experimental capabilities. *J. Synchrotron Radiat.* **26**, 1432–1447 (2019).
42. Nagarajan, K., Mallia, A. R., Reddy, V. S. & Hariharan, M. Access to triplet excited state in core-twisted perylenediimide. *J. Phys. Chem. C.* **120**, 8443–8450 (2016).
43. Sarkar, S. et al. Phosphorescence in bromobenzaldehyde can be enhanced through intramolecular heavy atom effect. *J. Phys. Chem. C.* **121**, 3771–3777 (2017).
44. Sunny, J. et al. Unveiling the intersystem crossing dynamics in N-annulated perylene bisimides. *Phys. Chem. Chem. Phys.* **25**, 28428–28436 (2023).
45. Toulson, B. W. et al. Probing ultrafast C-Br bond fission in the UV photochemistry of bromoform with core-to-valence transient absorption spectroscopy. *Struct. Dyn.* **6**, 054304 (2019).

46. Choi, E. H. et al. Filming ultrafast roaming-mediated isomerization of bismuth triiodide in solution. *Nat. Commun.* **12**, 4732 (2021).
47. Abma, G. L. et al. Direct observation of a roaming intermediate and its dynamics. *J. Am. Chem. Soc.* **146**, 12595–12600 (2024).
48. Suits, A. G. & Osborn, D. L. Twenty years of roaming reactions. *J. Phys. Chem. A* **128**, 10319–10321 (2024).
49. Kim, H. et al. Ultrafast structural dynamics of in-cage isomerization of diiodomethane in solution. *Chem. Sci.* **12**, 2114–2120 (2021).
50. Kjaer, K. S. et al. Introducing a standard method for experimental determination of the solvent response in laser pump, X-ray probe time-resolved wide-angle X-ray scattering experiments on systems in solution. *Phys. Chem. Chem. Phys.* **15**, 15003–15016 (2013).
51. Biasin, E. et al. Anisotropy enhanced X-ray scattering from solvated transition metal complexes. *J. Synchrotron Radiat.* **25**, 306–315 (2018).
52. Lee, J. H. et al. Transient X-ray diffraction reveals global and major reaction pathways for the photolysis of iodoform in solution. *Angew. Chem. Int Ed. Engl.* **47**, 1047–1050 (2008).
53. Kim, J. G. et al. Mapping the emergence of molecular vibrations mediating bond formation. *Nature* **582**, 520–524 (2020).
54. Kong, Q., Wulff, M., Lee, J. H., Bratos, S. & Ihee, H. Photochemical reaction pathways of carbon tetrabromide in solution probed by picosecond X-ray diffraction. *J. Am. Chem. Soc.* **129**, 13584–13591 (2007).
55. Ihee, H. et al. Ultrafast x-ray diffraction of transient molecular structures in solution. *Science* **309**, 1223–1227 (2005).
56. Ambrosio, F., Miceli, G. & Pasquarello, A. Redox levels in aqueous solution: Effect of van der Waals interactions and hybrid functionals. *J. Chem. Phys.* **143**, 244508 (2015).
57. Batatia, I., Kovács, D. P., Simm, G. N. C., Ortner, C. & Csányi, G. *MACE: Higher Order Equivariant Message Passing Neural Networks for Fast and Accurate Force Fields*. (2023).
58. Gaussian 16 Rev. C.01 (Wallingford, CT, 2016).
59. Yanai, T., Tew, D. P. & Handy, N. C. A new hybrid exchange–correlation functional using the Coulomb-attenuating method (CAM-B3LYP). *Chem. Phys. Lett.* **393**, 51–57 (2004).
60. Raghavachari, K. Perspective on "Density functional thermochemistry. III. The role of exact exchange. *Theor. Chem. Acc.: Theory, Comput., Modeling (Theoretica Chim. Acta* **103**, 361–363 (2000).

Acknowledgements

The authors acknowledge European XFEL in Schenefeld, Germany, for the provision of X-ray free-electron laser beamtime at FXE (proposal #3133, doi: 10.22003/XFEL.EU-DATA-003133-00) and thank the instrument and facility staff for assistance. This work was supported by the National Natural Science Foundation of China (T2495222); QK acknowledges Synchrotron Soleil. We acknowledge computing resources provided by the Information Technology Center of Shenzhen University of Advanced Technology (SUAT).

Author contributions

Q.K., M.W., T.W., and D.K. conceived and supervised the research. D.K., C.M., H.W., Y.J., P.S., K.Z., J.L., S.D., H.Y., P.Z., R.Z., X.L., Y.W., S.C., D.J., D.V., T.W., W.Y., and Q.K. performed the experiments. D.K., P.S., J.Z., W.Z., H.Y., and Q.K. performed the experimental data analysis and interpretation. M.L., J.Z., and J.L. performed AIMD simulations and DFT calculations. P.S., J.Z., D.K., and Q.K. wrote the paper, with contributions from all authors. All authors contributed to discussions about the content of the paper.

Competing interests

The authors declare no competing interests.

Additional information

Supplementary information The online version contains supplementary material available at https://doi.org/10.1038/s41467-026-69374-4.

Correspondence and requests for materials should be addressed to Wenkai Zhang, Jinggang Lan, Tsu-Chien Weng, Dmitry Khakhulin or Qingyu Kong.

Peer review information *Nature Communications* thanks Joel Bowman, and the other, anonymous, reviewer(s) for their contribution to the peer review of this work. A peer review file is available.